Journal of Materials Chemistry A



PAPER

View Article Online
View Journal



Cite this: DOI: 10.1039/d0ta02767g

Ultrahigh capacity 2D anode materials for lithium/ sodium-ion batteries: an entirely planar B_7P_2 monolayer with suitable pore size and distribution†

Changyan Zhu, Da Shiru Lin, Db Min Zhang, D*a Quan Li, Dc Zhongmin Su Dad and Zhongfang Chen D*b

Lithium-ion batteries (LIBs) are widely used energy storage devices, and sodium-ion batteries (SIBs) are promising alternatives to LIBs because sodium is of high abundance and low toxicity. However, a dominant obstacle for the advancement of LIBs and SIBs is the lack of high capacity anode materials, especially for SIBs. Here, we propose that three characteristics, namely appropriate pore size, suitable pore distribution, and an entirely planar topology, can help achieve ultrahigh capacity 2D anode materials. Under such guidelines, we constructed a B_7P_2 monolayer, and investigated its potential as a LIB/SIB anode material by means of density functional theory (DFT) computations. Encouragingly, the B_7P_2 monolayer possesses all the essential properties of a high-capacity LIB/SIB anode: its high stability ensures the experimental feasibility of synthesis, its metallicity does not change upon Li/Na adsorption and desorption, the Li/Na can well diffuse on the surface, and the open-circuit voltage is in a good range. Most importantly, the B_7P_2 monolayer has a high storage capacity of 3117 mA h g⁻¹ for both LIBs and SIBs, and this capacity value ranks among the highest for 2D SIB anode materials. This study offers us some good clues to design/discover other anode materials with ultrahigh capacities, and serves us another vivid example that (implicit and hidden) trends/rules in the literature can guide us in the design of functional materials more efficiently.

Received 10th March 2020 Accepted 27th April 2020

DOI: 10.1039/d0ta02767g

rsc.li/materials-a

Introduction

Rechargeable lithium-ion batteries (LIBs) are widely used in portable electronics and electric vehicles due to their merits of high energy densities, no memory effect, low self-discharge, and being environmentally benign.¹⁻⁴ Though both sodium-ion

batteries (SIBs) and LIBs were studied as early as in the 1970s, LIBs have been the focus due to their much higher energy densities. ⁵⁻⁸ Sharing similar chemical properties to lithium, sodium possesses some superior characteristics for battery applications, such as lower toxicity and higher earth abundance. Hence, SIBs have been resurrected as appealing candidates for medium and large-scale stationary energy storage. ⁹⁻¹³ One of the largest obstacles restricting SIBs' development and application is the limited anode storage capacity. ¹⁴⁻¹⁶ Therefore, it is indispensable to search for ultrahigh-storage anode materials for rechargeable LIBs and SIBs, especially SIBs, to satisfy the ever-growing demand for high-density energy storage equipment in the modern society. ¹⁷⁻²⁰

Two-dimensional (2D) materials are promising candidates for the next-generation LIB/SIB anode materials because of their high storage capacity, excellent electrical conductivity, and lower diffusion energy barrier. The performance of many 2D materials as anode materials has been explored, such as graphene and its derivatives, Transition-metal dichalcogenides, metal oxides, and transition-metal carbides. Particularly, sodium storage capacities have been significantly improved in several 2D materials, even reaching the same capacities as for lithium storage.

Our careful analysis of the reported 2D anode materials revealed that some characteristics, such as appropriate pore

[&]quot;Institute of Functional Material Chemistry, Faculty of Chemistry, National & Local United Engineering Laboratory for Power Battery, Northeast Normal University, Changchun 130024, China. E-mail: mzhang@nenu.edu.cn

^bDepartment of Chemistry, Institute for Functional Nanomaterials, University of Puerto Rico, Rio Piedras Campus, San Juan, PR 00931, USA. E-mail: zhongfangchen@gmail. com

State Key Laboratory of Superhard Materials, Key Laboratory of Automobile Materials of MOE, Department of Materials Science, Innovation Center for Computational Physics Method and Software, Jilin University, Changchun 130012, China

^dSchool of Chemistry and Environmental Engineering, Changchun University of Science and Technology, Changchun 130024, China

 $[\]dagger$ Electronic supplementary information (ESI) available: Maximum Na capacity of $\beta_{12}\text{-}borophene;$ validation of our computational methods; charge analysis; OCV of $B_7P_2(\text{Li/Na})_n;$ structural parameters, deformation electronic density, spin-polarized, snapshots of the B_7P_2 monolayer equilibrium structures at the end of AIMD simulations, details about the B_7P_2 bilayer, the ELF map of the B_7P_2 monolayer after adsorbing a single Li/Na atom, the electronic band structure of the B_7P_2 monolayer with different Li/Na adsorption ratios, snapshots of $B_7P_2(\text{Li/Na})_{16}$ at the end of AIMD simulations, and the most stable structures of $B_7P_2(\text{Li/Na})_n$. See DOI: 10.1039/d0ta02767g

size, suitable distance between adsorption sites, and an entirely planar topology, can greatly boost the Li/Na storage capacities. First, appropriate pore size and suitable distance between adsorption sites are crucial for porous 2D materials since the most favorable adsorption sites for Li/Na atoms are typically over the pores, instead of on top of certain atoms, as observed in all the examples containing pores, such as the porous B2S,67 BP, 69 InP₃, 66 TiC₃, 64 and NiC₃ (ref. 65) monolayers. Among them, the B2S and BP monolayers, as isoelectronic analogues of graphene, have a larger interval between the adjacent adsorption sites than graphene (3.03 Å and 3.18 Å vs. 2.47 Å), and consequently less repulsive interactions between the adsorbed Li/Na atoms, which lead to the possibility of forming a closely packed Li/Na layer on the B₂S and BP monolayers, and concomitant higher theoretical capacities for LIBs and SIBs. 67,69 Second, the entirely planar monolayer is beneficial to utilize more adsorption sites on the substrate. For example, the entirely planar NiC₃ monolayer (1698 mA h g⁻¹)⁶⁵ possesses higher specific capacity than the puckered TiC₃ monolayer (1278 mA h g⁻¹).⁶⁴ Compared with the puckered monolayer, the flattened planar structure can better reduce the repulsive interactions among the Na atoms adsorbed on the reasonably well separated adsorption sites, thus promoting the Na loading amounts. Moreover, the experimentally available boron monolayer materials, including the puckered triangular-borophene,70 the entirely planar striped borophene $(\beta_{12}$ -borophene)⁷¹ and χ_3 -borophene,⁷¹ are all proposed to be high-performance anode materials for LIBs and SIBs. Among them, the entirely planar and porous β_{12} -borophene and χ_3 -borophene were predicted to possess the same storage capacity (1984 mA h $\rm g^{-1}$ and 1240 mA h $\rm g^{-1}$) for LIBs and SIBs.68 However, the storage capacity of the puckered triangular-borophene for Na (2341 mA h g⁻¹) is obviously lower than that for Li (3306 mA h g⁻¹),72 and our computations showed that the entirely planar and porous β_{12} -borophene has a much higher Na storage capacity (3968 mA h g⁻¹) than the puckered triangular-borophene (2341 mA h g⁻¹) (Fig. S1 in the ESI†). Therefore, the entirely planar topology is a hidden key characteristic to further boost the Na storage capacities.

With the above rationale in mind, we looked back to the reported candidates of 2D anode materials for LIBs/SIBs. One inspiring material is the experimentally available striped borophene (β₁₂-borophene),⁷¹ which possesses the highest singlelayer storage capacity for SIBs. The high capacity of boron nanomaterials is attributed to the stronger binding interaction of the B₇-unit (than the B₆-unit) with Li/Na atoms and the longer distance between adjacent potential adsorption sites. Though with the same pore size and the same entirely planar topology, χ_3 -borophene has a lower Li/Na storage capacity than β_{12} -borophene,68 which is due to its shortage of B7-units. Therefore, introducing another element with bigger atomic ratio but having B₇-units allows us to tune the pore size and their distribution. Equally inspiring are black phosphorene, blue phosphorene, and the BP monolayer, and their superior capacities (865 mA h g⁻¹ in black phosphorene⁷³ and 865 mA h g⁻¹ in blue phosphorene⁷⁴ for SIBs, and 1283 mA h g⁻¹ in the BP monolayer69 for LIBs) strongly demonstrate the high potential of the P element as an anode material of LIBs and

SIBs. The exceptional Li/Na storage capacities of borophene and phosphorene prompted us to consider the B–P binary monolayers. Especially, a B_7P_2 binary monolayer, which can be constructed by replacing some C_6 -units in graphene with B_7 -units and substituting the remaining C atoms with P atoms (symmetry P6/mmm), caught our great attention (Fig. 1a), since the larger radius of P (relative to that of B) can help separate the B_7 -units, and the lone pair electron on P's p_z orbital is beneficial to stabilize the planar structure.

In this work, we systematically explored the potential of the B_7P_2 binary monolayer as a LIB/SIB anode material. This monolayer has high stability and is confirmed to be the global minimum in the 2D space, thus experimental realization is rather feasible. The B_7P_2 monolayer is metallic, its intrinsic metallicity is well retained at different Li/Na concentrations, and has low Li/Na diffusion barriers and small average opencircuit voltages. Most excitingly, its capacity for both LIBs and SIBs reaches 3117 mA h g⁻¹, especially its Na storage capacity is among the highest for 2D materials.⁷² All these unique and exceptional characteristics make the B_7P_2 monolayer a promising 2D ultrahigh capacity anode material for LIBs and SIBs. We also believe that our proposed principles can be used to design even more such anode materials.

2. Computational methods

The B₇P₂ monolayer is confirmed to be the global minimum by the particle-swarm optimization (PSO) method within the evolutionary scheme as implemented in the CALYPSO code,75 which is very effective in finding the ground or metastable structures at a given chemical composition.76-78 In our PSO simulation, the population size and the number of generations are both set to be 30. Unit cells containing 1, 2 and 4 formula units (f.u.) are considered. The structure optimizations and electronic property calculations are performed at the level of density functional theory (DFT) using the Vienna Ab initio Simulation Package (VASP).79 The Perdew-Burke-Ernzerhof (PBE) function with van der Waals (vdW) interaction proposed by Grimme (DFT-D2) is adopted.80,81 The projector augmentedwave (PAW) pseudopotential is utilized to represent electronion interactions. 82,83 A vacuum distance of 30 Å along the zdirection is used to avoid interactions between adjacent layers. A plane-wave cutoff energy of 600 eV is employed in all the computations. The convergence threshold is set as 10⁻⁶ eV in energy and 10^{-2} eV Å^{-1} in force. The Monkhorst-Pack k-point mesh resolution in reciprocal space is $2\pi \times 0.02 \text{ Å}^{-1}$. The hybrid Heyd-Scuseria-Ernzerhof (HSE06) functional is used to obtain more accurate density of states (DOS) and the band structure of the lowest-energy B₇P₂ monolayer.84

To evaluate the thermodynamic stability of the B_7P_2 monolayer, the cohesive energy $(E_{\rm coh})$ defined as $E_{\rm coh} = (7E_{\rm B} + 2E_{\rm P} - E_{\rm B_7P_2})/9$ is calculated, where $E_{\rm B}$, $E_{\rm P}$ and $E_{\rm B_7P_2}$ are the energies of the isolated B and P atoms and the B_7P_2 monolayer. To assess the kinetic stability, phonon dispersion of the B_7P_2 monolayer is computed using the finite displacement method as implemented in the PHONOPY program. To evaluate its thermal stability, *ab initio* molecular dynamics (AIMD) simulations

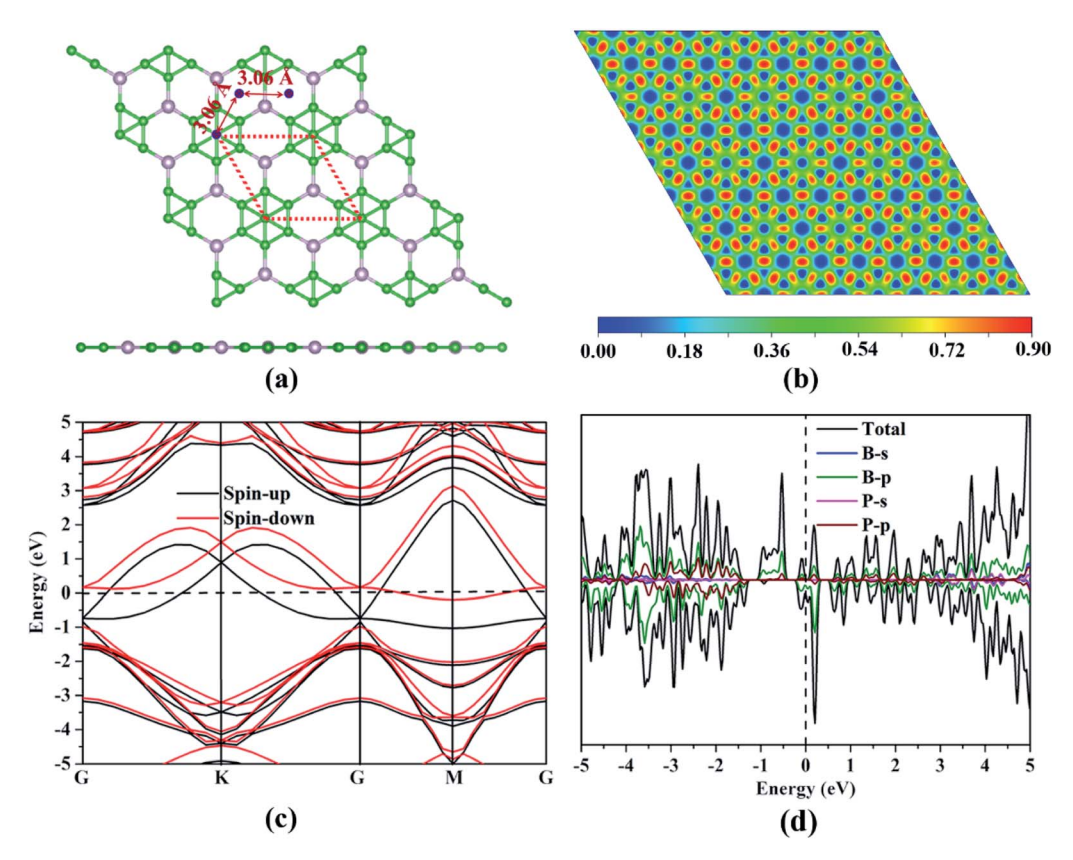


Fig. 1 (a) Optimized global minimum structure of the B_7P_2 monolayer. The red dashed lines indicate its primitive cell. (b) Electron localization function (ELF) map sliced in the (001) direction of the B₇P₂ monolayer, (c) electronic band structure of the B₇P₂ monolayer using the HSE06 functional, and (d) projected densities of states (PDOS) of the B_7P_2 monolayer using the HSE06 functional. The Fermi level is set to zero.

using the PBE functional and PAW pseudopotential are performed with a 3×3 supercell at different temperatures. AIMD simulations in an NVT ensemble last for 10 ps with a time step of 1.0 fs. The temperature is controlled by the Nose-Hoover thermostat.86

To investigate the Li and Na diffusion energy barrier on the B₇P₂ monolayer, the climbing-image nudged elastic band (CI-NEB) method is used to search for the minimum energy pathway between the given initial and final configurations.87

To evaluate if Li/Na atoms can be favorably adsorbed on the B₇P₂ monolayer to form B₇P₂(Li/Na)_n, we calculated both differential adsorption energy ($E_{\mathrm{ad\text{-}dif}}$) and average adsorption energy ($E_{\text{ad-ave}}$) of Li/Na atoms on the B_7P_2 monolayer. The differential adsorption energy for $B_7P_2(Li/Na)_n$, defined as E_{ad-dif} $=E_{B_7P_2(Li/Na)_n}-E_{B_7P_2(Li/Na)_{n-1}}-E_{Li/Na}$, describes the energy released/needed when adding one more Li/Na atom on the $B_7P_2(Li/Na)_{n-1}$ structure. According to this definition, a negative $E_{\text{ad-dif}}$ value suggests favorable adsorption; however, a small positive value does not exclude the formation of the next atom adsorption since this step can be considered as an activation barrier to overcome when forming the structure with one more adsorbed atom. The average adsorption energy for B₇P₂(Li/Na)_n is calculated using $E_{\text{ad-ave}} = (E_{B_7P_2(\text{Li/Na})_n} - E_{B_7P_2} - nE_{\text{Li/Na}})/n$, and a negative value indicates the thermodynamic preference of forming a specific B₇P₂(Li/Na)_n structure without metal atom clustering. Note that the volume and entropy changes during the adsorption process are neglected in our computations.

The average open-circuit voltage (OCV) is obtained by calculating the average voltage in the concentration range: V_{ave} $=-(E_{B_7P_2(Li/Na)_n}-E_{B_7P_2}-nE_{Li/Na})/ne$, in which $E_{B_7P_2(Li/Na)_n}$, $E_{B_7P_2}$, and $E_{\text{Li/Na}}$ are the energies of the B₇P₂ monolayer with adsorbed Li/Na atoms, the B₇P₂ monolayer in its global minimum, and a Li/Na atom in the body-centered cubic (bcc) structure.88

The maximum capacity C is calculated using C = 1000nF/(3600*M*) mA h g^{-1} , where *n* represents the maximum number of transferred electrons involved in the electrochemical process, F is the Faraday constant, and M is the mass of the B₇P₂ monolayer in g mol⁻¹.

3. Results and discussion

3.1. Structure, stability and electronic properties of the B₇P₂ monolayer - the global minimum in 2D space

Inspired by the obvious distinction between graphene and borophene as anode materials, we identified an eligible B₇P₂ monolayer satisfying the proposed criteria, which is confirmed to be the global minima through a comprehensive PSO search combined with first-principles calculations. The unit cell of the B₇P₂ monolayer consists of seven B atoms and two P atoms in the same plane with the optimized lattice constants of a = b =6.12 Å (Fig. 1a). In the B_7P_2 monolayer, one central B atom binds with six neighboring B atoms to form one B_7 -unit. The B–B distances in these B_7 -units (1.70 Å) are comparable to those in β_{12} -borophene (1.70 Å), which also consists of entirely planar B_7 -units. Meanwhile, each P atom binds with three B_7 -units, and each B_7 -unit is connected by six P atoms, forming a hexagonal B_4P_2 -unit with a pore diameter of 3.53 Å and B–P distance of 1.84 Å. Note that the lattice parameters and the pore diameter of the B_4P_2 -unit are both larger than those of graphene and borophenes (for the lattice parameters of graphene and borophenes, see Table S1 of the ESI†), which is beneficial to reduce the repulsive interactions among adsorbed Li/Na atoms according to our hypothesis, and is expected to help improve the Li/Na storage capacity.

To understand the bonding nature in the B_7P_2 monolayer, we plotted its electron localization function (ELF)⁸⁹ map in the (001) direction (Fig. 1b). Note that the values of 1.0 and 0.5 represent the perfect localization and the free electron-gas, while the value near zero denotes a low electron density area. For the B_7P_2 monolayer, an electron density of 0.9 around P atoms along three directions in the (001) direction suggests significant B–P covalent bonding. On the other hand, the other three π electrons in the B_7 -unit and the two electrons in the p_z orbital of the P atoms are delocalized in the whole monolayer framework with an electron density of around 0.25.

To understand the charge distribution of the B_7P_2 monolayer, we analyzed the deformation electronic density (DED). The deformation electronic density is defined as the difference between the total electronic density and the electronic density of the isolated atoms. Remarkable electron transfer occurs from the B_7 -unit to the P atoms (Fig. S2†), which can be confirmed by the Bader charge (-0.73|e| on each P atom) and Hirshfeld charge (-0.14|e| on each P atom) analyses. The covalent B-P σ bonds and delocalized π electrons in the whole framework guarantee its superior stability, and the unoccupied π orbitals in the B_7 -units are expected to benefit the electron diffusion upon Li/Na adsorption, as confirmed by our computations in Section 3.2.

Our computations also found that the B_7P_2 monolayer has a spin-polarized ferromagnetic ground state, which is 12.6 meV per unit cell lower in energy than the nonmagnetic state. The spin density distribution (Fig. S3†) shows that the spin-polarized electrons are mainly localized on the six peripheral B atoms of the B_7 -unit. The B_7P_2 monolayer is metallic, and the high electron density near the Fermi level is well revealed. The conducting nature mainly originates from the p orbitals of B atoms (Fig. 1c and d). The outstanding electronic conductivity is also beneficial for its application as a LIB/SIB anode material.

The B_7P_2 monolayer has superior thermodynamic, kinetic, thermal, and mechanical stabilities. The calculated cohesive energy of the B_7P_2 monolayer (5.49 eV per atom) is comparable to those of the experimentally available borophenes, including triangular-borophene (5.90 eV per atom),⁷⁰ β_{12} -borophene (5.95 eV per atom),⁷¹ and χ_3 -borophene (5.96 eV per atom),⁷¹ and it is much higher than that of phosphorene (3.48 eV per atom)⁹⁰ computed at the same theoretical level. Such a high cohesive energy suggests that the B_7P_2 monolayer is a strongly bonded network and has good thermodynamic stability. This monolayer

is also kinetically stable, as indicated by the absence of any imaginary frequency in the phonon dispersion curve in the whole Brillouin zone (Fig. S4†). Moreover, the B₇P₂ monolayer can well maintain its original configuration with the B7-units and the hexagonal B₄P₂-units up to 2000 K at the end of 10 ps MD simulations (the final snapshots of the B₇P₂ monolayer structures at temperatures of 500 K, 1000 K, 1500 K and 2000 K are given in Fig. S5†), and the distorted structures after MD simulations can restore the entirely planar structure upon full structural relaxation, indicating its high thermal stability. Furthermore, we evaluated the mechanical stability of the B₇P₂ monolayer. The calculated elastic constants of the B₇P₂ monolayer are $C_{11} = 175.24 \text{ N m}^{-1}$, $C_{22} = 173.37 \text{ N m}^{-1}$, $C_{12} = C_{21} = 173.37 \text{ N m}^{-1}$ 45.15 N m⁻¹ and $C_{66} = 63.79$ N m⁻¹, which satisfy the mechanical stability criteria: $C_{11}C_{22} - C_{12}^2 > 0$, $C_{66} > 0$. Thus, the B₇P₂ monolayer is mechanically stable. Though the in-plane Young's moduli (Y_a and Y_b) along a and b directions of the B_7P_2 monolayer (163.48 N m⁻¹ and 161.74 N m⁻¹, respectively) are less than that of graphene (341.60 N m⁻¹), 91 they are higher than the corresponding values of the experimentally available MoS₂ monolayer (126 N m⁻¹)⁹² and Cu₂Si monolayer (84.51 N m⁻¹), 93 suggesting that the B₇P₂ monolayer possesses promising potential for mechanical applications.

Finally, we examined the interlayer strength and stacking pattern when B_7P_2 monolayers are stacked together. Among the three considered bilayer stacking patterns (Fig. S6†), the complete overlap (AA) stacking bilayer is energetically the most favorable. Its computed interlayer energy (80 meV per atom at an interlayer distance of 2.85 Å) is even lower than the corresponding value (141 meV per atom at a distance of 3.08 Å) of the graphene bilayer. 94 Moreover, there is no obvious electron distribution between the upper-layer and lower-layer. These data indicate that B_7P_2 is inclined to be a monolayer, instead of stacking together to form multi-layers.

3.2. Li/Na adsorption and adatom diffusion on the B₇P₂ monolayer

To explore the potential of the B_7P_2 monolayer as an anode material for rechargeable LIBs and SIBs, first we investigated the single Li/Na atom adsorption and diffusion on the B_7P_2 monolayer. A 2 \times 2 supercell is used for the B_7P_2 monolayer, and three possible adsorption sites on the B_7P_2 monolayer, namely S1, S2 and S3 (Fig. 2a), are considered due to its high symmetry (P6/mmm). S1 locates over the center of the B_4P_2 -unit, or at the pore center; S2 is over the center of the B_7 -unit; and S3 is over the top site of the P atom.

The calculated Li/Na adsorption energies $(E_{\rm ad})$ on all these three adsorption sites are negative, suggesting that the process of single Li/Na atom adsorption on the $\rm B_7P_2$ monolayer is exothermic. Note that the energetically most favorable adsorption site for a single Li/Na atom is the S1 site above the pore center, with $E_{\rm ad}$ values of -1.54 and -1.41 eV for Li and Na, respectively. The preferential adsorption on the S1 site strongly supports our hypothesis that the existence of suitable pores would enhance the Li/Na adsorption. The S2 site is the second favorable position ($E_{\rm ad}$: -1.28 eV for Li, -1.20 eV for Na),

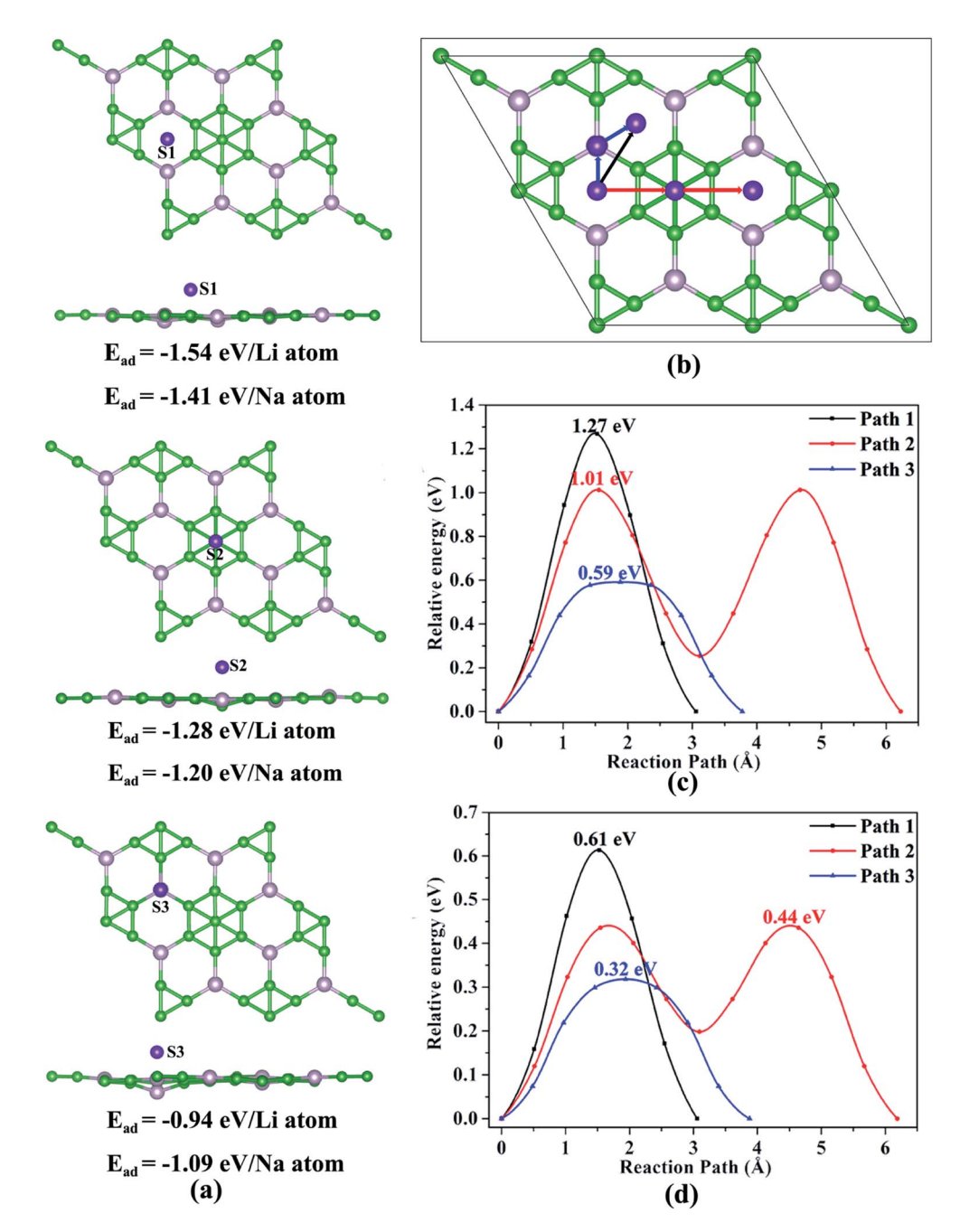


Fig. 2 (a) Optimized structures and the corresponding adsorption energy (E_{ad}) of single Li/Na atoms on three adsorption sites of the B_7P_2 monolayer, respectively. (b) Possible Li/Na diffusion pathways on the B_7P_2 monolayer; Paths 1, 2, and 3 are marked in black, red and blue. (c) Li and (d) Na diffusion energy barriers on the B_7P_2 monolayer.

followed by the S3 site ($E_{\rm ad}$: -0.94 eV for Li, -1.09 eV for Na). The short distance between S1 and S3 sites (1.77 Å) suggests that the adsorption on the S3 site is very likely unfavorable once the energetically most favorable S1 site is occupied.

After adsorption, significant charge transfer from the adsorbed Li/Na atoms to the B_7P_2 monolayer occurs, as indicated by the ELF map of the Li/Na adsorbed B_7P_2 monolayer (Fig. S7†), and the calculated Bader charge and Hirshfeld charge of the single Li/Na atoms on the monolayer (Table S2†). The electron transfer (0.8|e| according to Bader charge analysis) is comparable to that on borophenes, 68,95,96 which demonstrates

strong ionic interactions between the adsorbed Li/Na atoms and the substrate B_7P_2 monolayer.

To theoretically evaluate the charge/discharge rate of our newly proposed anode material, we investigated the diffusion pathways and the corresponding barriers of a single Li/Na ion on the B₇P₂ monolayer among different adsorption sites. In our computations, the energetically most preferred adsorption site, namely S1, is defined as the starting and the ending position for the Li/Na diffusion. Accordingly, there are three different diffusion pathways between two nearest neighboring adsorption sites (Fig. 2b): (i) Path 1, in which the adsorbed Li/Na

diffuses directly from one S1 site to another nearest S1 site; (ii) Path 2, in which the adsorbed Li/Na moves to another S1 site passing through its nearest S2 site; and (iii) Path 3, in which the adsorbed Li/Na transfers to another S1 site passing through its nearest S3 site. According to the calculated Li/Na diffusion barriers (Fig. 2c and d), Path 3 is the most optimal pathway for both Li and Na diffusion, and the Li/Na diffusion barriers (0.59 and 0.32 eV for Li and Na, respectively) are slightly lower than those on β_{12} -borophene and χ_3 -borophene,⁶⁷ and the corresponding Li/Na diffusion lengths are 3.77 Å and 3.88 Å, respectively. Notably, the S3 site is the highest energy point of the diffusion pathway along Path 3, which indicates that the adsorbed Li/Na cations can't accommodate on this adsorption site in practical applications. Though with the shortest possible distance, diffusion along Path 1 has the highest barriers (1.27 and 0.68 eV for Li and Na, respectively).

3.3. Maximum storage capacity and open-circuit voltage

We evaluated the maximum Li/Na storage capacity on the B_7P_2 monolayer through a gradient increment strategy by considering 16 different concentrations ($B_7P_2(\text{Li/Na})_n$, n=1–16). The most stable structures for the maximum Li/Na concentration, *i.e.*, with the stoichiometry of $B_7P_2(\text{Li/Na})_{16}$, are presented in Fig. 3b and c, while those at lower Li/Na concentrations are given in Fig. S8 and S9.† The entirely planar structure of the B_7P_2 monolayer is somewhat puckered once the adsorption site S2 is occupied by a Li/Na atom. Moreover, when the Li/Na atoms are adsorbed on the substrate, the lattice constants of the B_7P_2 monolayer are slightly changed (up to 1.8%, Table S5†). However, the slightly puckered structures and the lattice constants can quickly recover to the initial planar topography when the Li/Na atoms are removed from the B_7P_2 monolayer.

We calculated both the differential adsorption energy $(E_{\rm ad-dif})$ and average adsorption energy $(E_{\rm ad-ave})$ values at different lithiation/sodiation levels, as presented in Fig. 3a and Table S6.† In general, the differential adsorption energy and average adsorption energy feature the same trend: both fluctuate and approach zero when increasing the number of adsorbed Li/Na atoms. The calculated $E_{\rm ad-ave}$ values are all negative and lower than the $E_{\rm ad-dif}$ values, and only a few $E_{\rm ad-dif}$ values are slightly positive (the

maximum values are +0.25 eV for $B_7P_2Li_{12}$ and +0.20 eV for $B_7P_2Na_{15}$). At the highest concentration, $B_7P_2(Li/Na)_{16}$, the calculated average adsorption energies are -0.28 eV per Li atom and -0.24 eV per Na atom, respectively, suggesting that the lithiated/sodiated monolayer does not suffer the metal clustering problem, in other words, the Li/Na atoms prefer being adsorbed separately on the B_7P_2 monolayer even at such a high Li/Na ratio. Thus, we expect that the maximum storage capacity can reach 3117 mA h g⁻¹ with the stoichiometry of $B_7P_2(Li/Na)_{16}$.

Is the highly lithiated/sodiated B_7P_2 monolayer thermally stable? To address this question, we performed AIMD simulations of $B_7P_2\mathrm{Li}_{16}$ and $B_7P_2\mathrm{Na}_{16}$ with a 3 \times 3 supercell at a temperature of 300 K. Encouragingly, the adsorbed Li/Na atoms are well attached to the B_7P_2 monolayer after 10 ps simulations (Fig. S10†), and the slightly puckered $B_7P_2(\mathrm{Li/Na})_{16}$ at the end of MD simulations can quickly recover to the initial planar topography when the Li/Na atoms are removed from the B_7P_2 monolayer. Thus, the B_7P_2 monolayer is structurally stable even after high lithiation/sodiation, which is beneficial for recharging LIBs and SIBs.

Notably, the maximum theoretical storage capacity of the B_7P_2 monolayer (corresponding to $B_7P_2(Li/Na)_{16}$) is 3117 mA h g^{-1} , which is roughly comparable with that of triangular-borophene for Li, and reaches a new record for Na among the reported 2D materials (372 mA h g⁻¹ of graphite for Li, ²⁹ 1498 mA h g⁻¹ of B₂S monolayer for Li/Na, ⁶⁷ 1283 mA h g⁻¹ of BP monolayer for Li, 69 3306 mA h g^{-1} of triangular-borophene for Li,⁷² 2341 mA h g⁻¹ of triangular-borophene for Na,⁷² 1984 mA h g^{-1} of β_{12} -borophene for Li/Na,⁶⁸ 1240 mA h g^{-1} of $\chi_3\text{-borophene}$ for Li/Na, 68 1278 mA h g^{-1} of TiC $_3$ monolayer for $Na,^{64}$ and 1698 mA h g^{-1} of NiC_3 monolayer for Li/Na⁶⁵). Such high storage capacities for Li and Na, especially for Na, further validate our hypothesis that the latent characteristics, namely appropriate pore size, suitable distance between adsorption sites, and an entirely planar topology of 2D anode materials, can greatly boost the Li/Na storage capacities.

In addition, the inherent metallicity of the B_7P_2 monolayer is well preserved at different Li/Na concentrations (Fig. S11 and S12†), which is important for charge–discharge cycles. The calculated $B_7P_2(\text{Li/Na})_n$ (n=1–16) are all metallic, expect

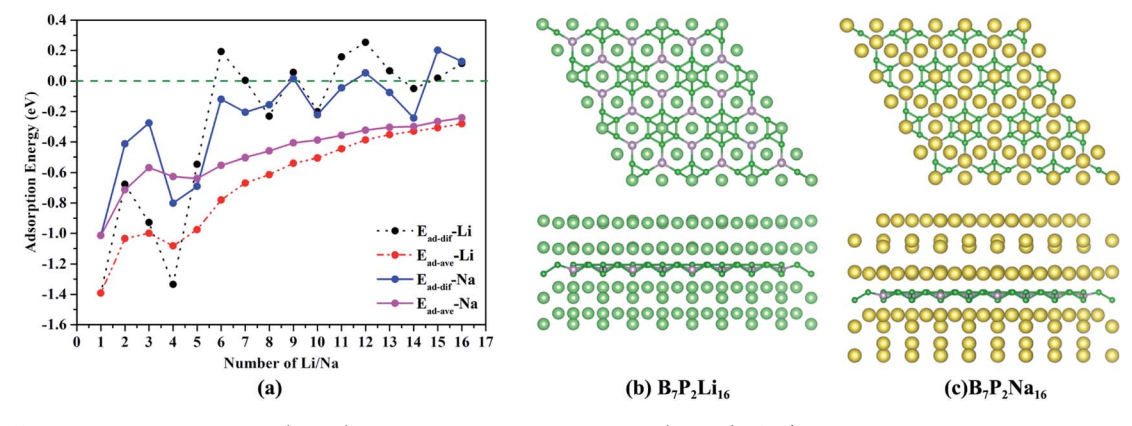


Fig. 3 (a) Differential adsorption energy ($E_{\rm ad-dif}$) and average adsorption energy ($E_{\rm ad-ave}$) of Li/Na atoms on the B_7P_2 monolayer. Top and side views of the most stable structure with the maximum (b) Li and (c) Na concentration on the B_7P_2 monolayer.

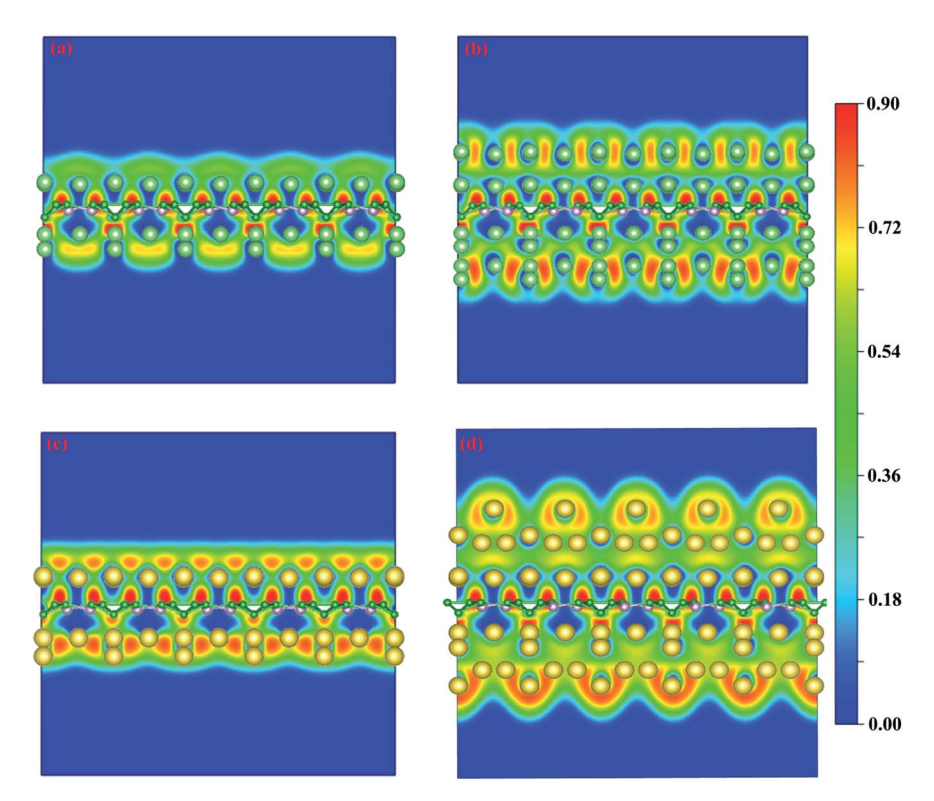


Fig. 4 ELF maps sliced in the (100) direction of the B_7P_2 monolayer with (a) one layer of Li atoms ($B_7P_2Li_8$), (b) two layers of Li atoms ($B_7P_2Li_{16}$), (c) one layer of Na atoms ($B_7P_2Na_8$), and (d) two layers of Na atoms ($B_7P_2Na_{16}$).

B₇P₂Li₅ and B₇P₂Na₅ with small band gaps (0.43 eV and 0.09 eV, respectively). In comparison, the recently predicted anode material for Na-ion batteries, a P₃C monolayer, has a band gap of 0.77 eV upon sodiation to P₃CNa.97

To understand the origin of the high Li/Na storage capacities and the multi-layer adsorption behavior, we compared the ELF maps sliced in the (100) direction of the B₇P₂ monolayer with two representative Li/Na adsorption concentrations, i.e., B₇P₂(Li/Na)₈ with one layer of Li/Na atoms and B₇P₂(Li/Na)₁₆ with two layers of Li/Na atoms (Fig. 4). Clearly, more electrons are transferred from the inner layer to the outer layer. Moreover, the dispersive electrons are well spread out in the metal layers, forming a negative electron cloud, which can effectively decrease the repulsion interactions among the adsorbed Li/Na atoms and stabilize the outer-layer Li/Na atoms.98,99 A similar phenomenon was observed for the multi-layer Na atom adsorption in the MoN2 monolayer.100

The theoretical open-circuit voltage (OCV) values, as another important parameter to evaluate the performance of anode materials, are in the range of 0.24-1.39 V at the 16 different Li/ Na concentrations examined here (Table S3†). Such OCV values are also beneficial for our predicted anode material, since it will result in a larger cathode-anode voltage difference, and thus a higher cell voltage.

Conclusions

Our analysis of the reported 2D anode materials revealed that some characteristics, namely appropriate pore size, suitable distance between adsorption sites, and an entirely planar topology, could boost the Li/Na storage capacity, and thus help achieve ultrahigh capacity anode materials for LIBs and SIBs. Guided by these insights and encouraged by recent discoveries of using borophene and phosphorene as high-performance LIB/SIB anode materials, we constructed the B₇P₂ monolayer with similar topologies to borophene by combining the B7-units in borophene and the P element with a larger atomic radius. Our computations showed that the proposed structure is the global minimum in the 2D space and possesses the essential properties as a promising ultrahigh capacity LIB/SIB anode material: it has superior thermodynamic, kinetic, thermal and mechanical stabilities, preserves its intrinsic metallicity upon Li/Na adsorption and desorption, and has a high Li/Na mobility and relatively small average open-circuit voltages. Encouragingly, its capacity (3117 mA h g^{-1}) is eight times higher than that of the commercial graphite for LIBs, and among the highest for 2D SIB anode materials.

We strongly encourage further studies of purely planar 2D materials containing high abundance of reasonably well separated pores with suitable sizes, which are promising candidates for ultrahigh capacity LIB/SIB anode materials, and believe that revealing the trends/rules in the vast literature, which may be implicit or hidden, will greatly accelerate our materials discovery process.

Conflicts of interest

There are no conflicts to declare.

Acknowledgements

The work is financially supported in China by the National Natural Science Foundation of China (21673036 and 21771035) and in the USA by the NSF Center for the Advancement of Wearable Technologies (Grant 1849243) and by the NASA MIRO-Puerto Rico Space Partnership for Research, Education and Training (PR-SPRINT) under grant # 80NSSC19M0236. Most computations were carried out on TianHe-2 at the LvLiang Cloud Computing Center of China. We acknowledge the support of the computational resources from the Institute of Theoretical Chemistry, Jilin University. In addition, we are grateful to the MatCloud (http://matcloud.cnic.cn) for discussion and computational support.

References

- 1 D. P. Dubal, O. Ayyad, V. Ruiz and P. Gomez-Romero, *Chem. Soc. Rev.*, 2015, 44, 1777–1790.
- 2 J. W. Choi and D. Aurbach, Nat. Rev. Mater., 2016, 1, 16013.
- 3 S. Hy, H. Liu, M. Zhang, D. Qian, B. J. Hwang and Y. S. Meng, *Energy Environ. Sci.*, 2016, **9**, 1931–1954.
- 4 M. Li, J. Lu, Z. Chen and K. Amine, *Adv. Mater.*, 2018, 30, 1800561.
- 5 N. Oyama, T. Tatsuma, T. Sato and T. Sotomura, *Nature*, 1995, 373, 598.
- 6 Y. Idota, T. Kubota, A. Matsufuji, Y. Maekawa and T. Miyasaka, *Science*, 1997, 276, 1395–1397.
- 7 M. Armand and J. M. Tarascon, Nature, 2008, 451, 652.
- 8 P. Simon, Y. Gogotsi and B. Dunn, *Science*, 2014, **343**, 1210–1211
- 9 S. W. Kim, D. H. Seo, X. Ma, G. Ceder and K. Kang, Adv. Energy Mater., 2012, 2, 710–712.
- 10 V. Palomares, P. Serras, I. Villaluenga, K. B. Hueso, J. Carretero-González and T. Rojo, *Energy Environ. Sci.*, 2012, 5, 5884–5901.
- 11 M. D. Slater, D. Kim, E. Lee and C. S. Johnson, Adv. Funct. Mater., 2013, 23, 947–958.
- 12 Y. Liang, W. H. Lai, Z. Miao and S. L. Chou, *Small*, 2018, **14**, 1702514.
- 13 C. Delmas, Adv. Energy Mater., 2018, 8, 1703137.
- 14 N. Yabuuchi, K. Kubota, M. Dahbi and S. Komaba, *Chem. Rev.*, 2014, **114**, 11636–11682.
- 15 D. Kundu, E. Talaie, V. Duffort and L. F. Nazar, *Angew. Chem., Int. Ed.*, 2015, 54, 3431–3448.
- 16 P. K. Nayak, L. Yang, W. Brehm and P. Adelhelm, *Angew. Chem., Int. Ed.*, 2018, 57, 102–120.
- 17 M. Winter and R. J. Brodd, *Chem. Rev.*, 2004, **104**, 4245–4269.
- 18 V. Etacheri, R. Marom, R. Elazari, G. Salitra and D. Aurbach, Energy Environ. Sci., 2011, 4, 3243–3262.
- 19 J. Sun, H. W. Lee, M. Pasta, H. Yuan, G. Zheng, Y. Sun, Y. Li and Y. Cui, *Nat. Nanotechnol.*, 2015, **10**, 980–986.
- 20 M. Lao, Y. Zhang, W. Luo, Q. Yan, W. Sun and S. X. Dou, *Adv. Mater.*, 2017, **29**, 1700622.
- 21 H. Cui, Y. Guo, W. Ma and Z. Zhou, ChemSusChem, 2020, 13, 1155–1171.

- 22 Y. Jing, Z. Zhou, C. R. Cabrera and Z. Chen, *J. Mater. Chem. A*, 2014, **2**, 12104–12122.
- 23 A. Gupta, T. Sakthivel and S. Seal, *Prog. Mater. Sci.*, 2015, 73, 44–126.
- 24 L. Shi and T. Zhao, J. Mater. Chem. A, 2017, 5, 3735-3758.
- 25 D. Wu, Y. Li and Z. Zhou, *Theor. Chem. Acc.*, 2011, **130**, 209–213.
- 26 A. L. M. Reddy, A. Srivastava, S. R. Gowda, H. Gullapalli, M. Dubey and P. M. Ajayan, ACS Nano, 2010, 4, 6337–6342.
- 27 X. Fan, W. Zheng and J. L. Kuo, ACS Appl. Mater. Interfaces, 2012, 4, 2432-2438.
- 28 V. Chabot, D. Higgins, A. Yu, X. Xiao and Z. Chen, *Energy Environ. Sci.*, 2014, 7, 1564–1596.
- 29 X. Wang, Q. Weng, X. Liu, X. Wang, D. M. Tang, W. Tian, C. Zhang, W. Yi, D. Liu and Y. Bando, *Nano Lett.*, 2014, 14, 1164–1171.
- 30 O. I. Malyi, K. Sopiha, V. V. Kulish, T. L. Tan, S. Manzhos and C. Persson, *Appl. Surf. Sci.*, 2015, 333, 235–243.
- 31 B. Luo and L. Zhi, Energy Environ. Sci., 2015, 8, 456-477.
- 32 M. Zhou, X. Li, B. Wang, Y. Zhang, J. Ning, Z. Xiao, X. Zhang, Y. Chang and L. Zhi, *Nano Lett.*, 2015, **15**, 6222–6228.
- 33 L. Zhou, Z. Hou, B. Gao and T. Frauenheim, *J. Mater. Chem. A*, 2016, 4, 13407–13413.
- 34 J. Yang, X. Zhou, D. Wu, X. Zhao and Z. Zhou, *Adv. Mater.*, 2017, 29, 1604108.
- 35 Y. Li, D. Wu, Z. Zhou, C. R. Cabrera and Z. Chen, *J. Phys. Chem. Lett.*, 2012, 3, 2221–2227.
- 36 M. Pumera, Z. Sofer and A. Ambrosi, J. Mater. Chem. A, 2014, 2, 8981–8987.
- 37 T. Stephenson, Z. Li, B. Olsen and D. Mitlin, *Energy Environ. Sci.*, 2014, 7, 209–231.
- 38 R. Bhandavat, L. David and G. Singh, *J. Phys. Chem. Lett.*, 2012, 3, 1523–1530.
- 39 B. Qu, C. Ma, G. Ji, C. Xu, J. Xu, Y. S. Meng, T. Wang and J. Y. Lee, *Adv. Mater.*, 2014, **26**, 3854–3859.
- 40 H. Jiang, D. Ren, H. Wang, Y. Hu, S. Guo, H. Yuan, P. Hu, L. Zhang and C. Li, Adv. Mater., 2015, 27, 3687–3695.
- 41 E. Yang, H. Ji and Y. Jung, J. Phys. Chem. C, 2015, 119, 26374–26380.
- 42 X. Wang, Q. Weng, Y. Yang, Y. Bando and D. Golberg, *Chem. Soc. Rev.*, 2016, 45, 4042–4073.
- 43 D. B. Putungan, S. H. Lin and J. L. Kuo, *ACS Appl. Mater. Interfaces*, 2016, **8**, 18754–18762.
- 44 C. Arrouvel, S. C. Parker and M. S. Islam, *Chem. Mater.*, 2009, **21**, 4778–4783.
- 45 J. Procházka, L. Kavan, M. Zukalová, O. Frank, M. Kalbáč, A. T. Zukal, M. Klementová, D. Carbone and M. Graetzel, Chem. Mater., 2009, 21, 1457–1464.
- 46 T. Beuvier, M. Richard-Plouet, M. Mancini-Le Granvalet, T. Brousse, O. Crosnier and L. Brohan, *Inorg. Chem.*, 2010, 49, 8457–8464.
- 47 A. S. Dalton, A. A. Belak and A. Van der Ven, *Chem. Mater.*, 2012, **24**, 1568–1574.
- 48 A. G. Dylla, P. Xiao, G. Henkelman and K. J. Stevenson, *J. Phys. Chem. Lett.*, 2012, **3**, 2015–2019.

- 49 S. Liu, H. Jia, L. Han, J. Wang, P. Gao, D. Xu, J. Yang and S. Che, Adv. Mater., 2012, 24, 3201-3204.
- 50 A. G. Dylla, G. Henkelman and K. J. Stevenson, Acc. Chem. Res., 2013, 46, 1104-1112.
- 51 H. Sugaya, K. Fukuda, M. Morita, H. Murayama, E. Matsubara, T. Kume and Y. Uchimoto, Chem. Lett., 2015, 44, 1595-1597.
- 52 J. Ni, Y. Zhao, L. Li and L. Mai, Nano Energy, 2015, 11, 129-135.
- 53 M. Liu, C. Yan and Y. Zhang, Sci. Rep., 2015, 5, 8326.
- 54 Q. Tang, Z. Zhou and P. Shen, J. Am. Chem. Soc., 2012, 134, 16909-16916.
- 55 M. Naguib, J. Halim, J. Lu, K. M. Cook, L. Hultman, Y. Gogotsi and M. W. Barsoum, J. Am. Chem. Soc., 2013, 135, 15966-15969.
- 56 Y. Xie, M. Naguib, V. N. Mochalin, M. W. Barsoum, Y. Gogotsi, X. Yu, K. W. Nam, X. Q. Yang, A. I. Kolesnikov and P. R. Kent, J. Am. Chem. Soc., 2014, 136, 6385-6394.
- 57 D. Sun, Q. Hu, J. Chen, X. Zhang, L. Wang, Q. Wu and A. Zhou, ACS Appl. Mater. Interfaces, 2015, 8, 74-81.
- 58 E. Yang, H. Ji, J. Kim, H. Kim and Y. Jung, Phys. Chem. Chem. Phys., 2015, 17, 5000-5005.
- 59 Q. Sun, Y. Dai, Y. Ma, T. Jing, W. Wei and B. Huang, J. Phys. Chem. Lett., 2016, 7, 937-943.
- 60 J. Halim, S. Kota, M. R. Lukatskaya, M. Naguib, M. Q. Zhao, E. J. Moon, J. Pitock, J. Nanda, S. J. May and Y. Gogotsi, Adv. Funct. Mater., 2016, 26, 3118-3127.
- 61 M. Ashton, R. G. Hennig and S. B. Sinnott, Appl. Phys. Lett., 2016, 108, 023901.
- 62 Z. Xu, X. Lv, J. Chen, L. Jiang, Y. Lai and J. Li, Phys. Chem. Chem. Phys., 2017, 19, 7807-7819.
- 63 T. Yu, S. Zhang, F. Li, Z. Zhao, L. Liu, H. Xu and G. Yang, J. Mater. Chem. A, 2017, 5, 18698-18706.
- 64 T. Yu, Z. Zhao, L. Liu, S. Zhang, H. Xu and G. Yang, J. Am. Chem. Soc., 2018, 140, 5962-5968.
- 65 C. Zhu, X. Qu, M. Zhang, J. Wang, Q. Li, Y. Geng, Y. Ma and Z. Su, J. Mater. Chem. A, 2019, 7, 13356-13363.
- 66 J. Liu, C. S. Liu, X. J. Ye and X. H. Yan, J. Mater. Chem. A, 2018, 6, 3634-3641.
- 67 P. Li, Z. Li and J. Yang, J. Phys. Chem. Lett., 2018, 9, 4852-4856.
- 68 X. Zhang, J. Hu, Y. Cheng, H. Y. Yang, Y. Yao and S. A. Yang, Nanoscale, 2016, 8, 15340-15347.
- 69 H. Jiang, W. Shyy, M. Liu, L. Wei, M. Wu and T. Zhao, J. Mater. Chem. A, 2017, 5, 672-679.
- 70 A. J. Mannix, X. F. Zhou, B. Kiraly, J. D. Wood, D. Alducin, B. D. Myers, X. Liu, B. L. Fisher, U. Santiago and J. R. Guest, Science, 2015, 350, 1513-1516.
- 71 B. Feng, J. Zhang, Q. Zhong, W. Li, S. Li, H. Li, P. Cheng, S. Meng, L. Chen and K. Wu, Nat. Chem., 2016, 8, 563.
- 72 D. W. Rao, L. Y. Zhang, Z. S. Meng, X. R. Zhang, Y. H. Yang, G. J. Qiao, X. Q. Shen, H. Xia, J. H. Liu and R. F. Lu, J. Mater. Chem. A, 2017, 5, 2328-2338.
- 73 V. Kulish, O. Malyi, C. Persson and P. Wu, Phys. Chem. Chem. Phys., 2015, 17, 13921-13928.

- 74 S. Mukherjee, L. Kavalsky and C. Singh, ACS Appl. Mater. Interfaces, 2018, 10, 8630-8639.
- 75 Y. Wang, J. Lv, L. Zhu and Y. Ma, Phys. Rev. B: Condens. Matter Mater. Phys., 2010, 82, 094116.
- 76 X. Wu, J. Dai, Y. Zhao, Z. Zhuo, J. Yang and X. C. Zeng, ACS Nano, 2012, 6, 7443-7453.
- 77 L. M. Yang, V. Bačić, I. A. Popov, A. I. Boldyrev, T. Heine, T. Frauenheim and E. Ganz, J. Am. Chem. Soc., 2015, 137, 2757-2762.
- 78 C. Zhu, H. Lv, X. Qu, M. Zhang, J. Wang, S. Wen, Q. Li, Y. Geng, Z. Su and X. Wu, J. Mater. Chem. C, 2019, 7, 6406-6413.
- 79 G. Kresse and J. Hafner, Phys. Rev. B: Condens. Matter Mater. Phys., 1993, 47, 558.
- 80 J. P. Perdew, K. Burke and M. Ernzerhof, Phys. Rev. Lett., 1996, 77, 3865.
- 81 S. Grimme, *I. Comput. Chem.*, 2004, 25, 1463-1473.
- 82 P. E. Blöchl, Phys. Rev. B: Condens. Matter Mater. Phys., 1994, **50**, 17953.
- 83 G. Kresse, Phys. Rev. B: Condens. Matter Mater. Phys., 1999, **59**, 1758.
- 84 J. Heyd, G. E. Scuseria and M. Ernzerhof, J. Chem. Phys., 2003, 118, 8207-8215.
- 85 A. Togo, F. Oba and I. Tanaka, Phys. Rev. B: Condens. Matter Mater. Phys., 2008, 78, 134106.
- 86 G. J. Martyna, M. L. Klein and M. Tuckerman, J. Chem. Phys., 1992, 97, 2635-2643.
- 87 G. Mills and H. Jónsson, Phys. Rev. Lett., 1994, 72, 1124.
- 88 M. Hanfland, I. Loa and K. Syassen, Phys. Rev. B: Condens. Matter Mater. Phys., 2002, 65, 184109.
- 89 A. Savin, R. Nesper, S. Wengert and T. F. Fässler, Angew. Chem., Int. Ed., 1997, 36, 1808-1832.
- 90 H. Liu, A. T. Neal, Z. Zhu, Z. Luo, X. Xu, D. Tománek and P. D. Ye, ACS Nano, 2014, 8, 4033-4041.
- 91 Q. Peng, X. Wen and S. De, RSC Adv., 2013, 3, 13772.
- 92 Y. Cai, G. Zhang and Y. W. Zhang, J. Am. Chem. Soc., 2014, 136, 6269-6275.
- 93 L. Yang, V. Bačić, I. A. Popov, A. I. Boldyrev, T. Heine, T. Frauenheim and E. Ganz, J. Am. Chem. Soc., 2015, 137, 2757-2762.
- 94 R. W. G. Wyckoff, Crystal Structures, Interscience Publishers, New York, 2nd edn, 1963, vol. 1, p. 7.
- 95 H. Jiang, Z. Lu, M. Wu, F. Ciucci and T. Zhao, Nano Energy, 2016, 23, 97-104.
- 96 P. Liang, Y. Cao, B. Tai, L. Zhang, H. Shu, F. Li, D. Chao and X. Du, J. Alloys Compd., 2017, 704, 152-159.
- 97 Z. Zhao, T. Yu, S. Zhang, H. Xu, G. Yang and Y. Liu, J. Mater. Chem. A, 2019, 7, 405-411.
- 98 Y. Ma, M. Eremets, A. R. Oganov, Y. Xie, I. Trojan, S. Medvedev, A. O. Lyakhov, M. Valle and V. Prakapenka, Nature, 2009, 458, 182.
- 99 M. S. Miao and R. Hoffmann, J. Am. Chem. Soc., 2015, 137, 3631-3637.
- 100 X. Zhang, Z. Yu, S. S. Wang, S. Guan, H. Y. Yang, Y. Tao and S. A. Yang, J. Mater. Chem. A, 2016, 4, 15224-15231.